remote sensing

MDPI

Article

Accuracy and Precision of Shallow-Water Photogrammetry from the Sea Surface

Elisa Casella [1,*], Giovanni Scicchitano [2] and Alessio Rovere [1,3]

[1] DAIS, Department for Environmental Sciences, Statistics and Informatics, Ca' Foscari University of Venice, 30172 Venice, Italy
[2] Department of Earth and Geoenvironmental Sciences, University of Bari Aldo Moro, 70121 Bari, Italy
[3] MARUM, Center for Marine Environmental Sciences, University of Bremen, 28359 Bremen, Germany
* Correspondence: elisa.casella@unive.it

Abstract: Mapping shallow-water bathymetry and morphology represents a technical challenge. In fact, acoustic surveys are limited by water depths reachable by boat, and airborne surveys have high costs. Photogrammetric approaches (either via drone or from the sea surface) have opened up the possibility to perform shallow-water surveys easily and at accessible costs. This work presents a simple, low-cost, and highly portable platform that allows gathering sequential photos and echosounder depth values of shallow-water sites (up to 5 m depth). The photos are then analysed in conjunction with photogrammetric techniques to obtain digital bathymetric models and orthomosaics of the seafloor. The workflow was tested on four repeated surveys of the same area in the Western Mediterranean and allowed obtaining digital bathymetric models with centimetric average accuracy and precision and root mean square errors within a few decimetres. The platform presented in this work can be employed to obtain first-order bathymetric products, enabling the contextual establishment of the depth accuracy of the final products.

Keywords: shallow-water bathymetry; underwater topography; bathymetric survey

Citation: Casella, E.; Scicchitano, G.; Rovere, A. Accuracy and Precision of Shallow-Water Photogrammetry from the Sea Surface. *Remote Sens.* **2024**, *16*, 4321. https://doi.org/10.3390/rs16224321

Academic Editors: Jaroslaw Tegowski and Deepak R. Mishra

Received: 25 September 2024
Revised: 8 November 2024
Accepted: 15 November 2024
Published: 19 November 2024

1. Introduction

Mapping seabed bathymetry and morphology is among the most challenging tasks for coastal surveyors and was developed only in the last century, with the improvement and standardisation of acoustic methods [1]. Despite significant advancements in acoustic surveys and positioning systems over the past decades, substantial limitations remain in the application of these techniques for surveys in shallow coastal environments [2].

In shallow water, multi-beam echo sounder (MBES) systems fail to provide adequate seabed coverage for detailed morphological mapping [3]. Other acoustic techniques, such as side scan sonar (SSS) systems, frequently struggle to achieve the correct geometries, even at high frequencies, resulting in considerable noise in the recordings and distortions in seabed feature representation [4,5]. Moreover, in shallow-waters, SSS systems encounter considerable challenges in acoustic positioning, often necessitating manual layback adjustments, leading to significant positional inaccuracies in mapping the seabed morphology [6].

While acoustic methods, such as MBES and SSS (from either boats or autonomous underwater vehicles), remain the more reliable way of mapping bathymetry in deep waters, a number of techniques, either alternative or complementary to acoustics, are available for shallow water areas (i.e., less than 10 m depth). Among these, airborne laser bathymetry (light detection and ranging, LiDAR) was first developed in the 1960s and 1970s [1] and is now routinely employed to survey coastal bathymetry (e.g., Harris et al. [7]), where the use of boats for acoustic surveying is impractical (e.g., due to waters too shallow to allow safe navigation) or when autonomous surface vehicles (such as those described by Giordano et al. [8] or Sotelo-Torres et al. [9]) are not available. Alongside airborne

LiDAR, satellite-derived bathymetry (ground-truthed with acoustic bathymetric data) has started to be largely used to survey areas with highly transparent waters such as coral reefs (e.g., Collin et al. [10]). Thanks to the first spaceborne photon-counting LiDAR mounted on the ICESat-2 satellite, as of 2018 shallow-water satellite-derived bathymetry can also be carried out exclusively with remotely sensed data, coupling multispectral imagery with transects of seabed depths measured by ICESat-2 [11], in the areas where data from the latter are available.

The spreading of unoccupied aircraft systems (UAS) has favoured the development of new bathymetric mapping techniques. These are based on the analysis of multispectral imagery [12,13], or structure from motion/multi-view stereo (SfM/MVS) techniques (e.g., Casella et al. [14,15]), with various strategies to solve the issues caused by refraction at the air/sea interface [16,17]. SfM/MVS has seen an exponential increase in applications in the last decade [18] and proved a reliable technique to map shallow-water bathymetry from UAS imagery taken above clear and calm waters, reaching accuracies lower than traditional sounding techniques (e.g., David et al. [19]) but still useful for environmental applications (e.g., Casella et al. [15], Fallati et al. [20]).

SfM/MVS approaches can also be used on images taken directly underwater or from the sea surface, thus avoiding the issues related to refraction caused by the air/sea interface [17] but not those due to poor water transparency and caustics, i.e., the projection of rays of sunlight on the seafloor causing varying patterns that may affect the identification of tie points on the seafloor by SfM/MVS algorithms [21,22]. Applications of underwater SfM/MVS are widespread in several fields where shallow-water mapping of objects on the seafloor (and their change through time) is key, such as archeology [23–25] or ecology [26–29]. Within this field, protocols for habitat mapping using SfM/MVS are developing [30], also including mixed approaches merging aerial and water surface platforms [31,32].

There are two main types of underwater SfM/MVS that depend on the location from which the camera is operated. In one case, the camera is fully submerged and is operated by a diver that either follows a pre-defined path [33–35] or takes overlapping pictures of an object of interest [36]. In the second case, the camera is fixed to a floating device on the sea surface and acquires images of the seafloor following a grid pattern [28,37]. While unoccupied surface vehicles (USVs), either towed or following pre-programmed routes, are starting to be employed for this kind of mapping [38], systems composed of a floating platform dragged by a swimmer [37,39] remain the simplest and more cost-effective tools.

The most low-cost and easily deployable surface platform was recently described by Jaud et al. [37], who used a floating device (called POSEIDON) with an aluminium frame where two GoPro cameras (one of which is optional) are mounted and aligned with a real-time kinematics (RTK) GNSS system. Overall, they estimated the cost of POSEIDON at 1500 $. While their work showed that using SfM/MVS to map shallow-water areas from the surface is fast and reliable, with some trade-offs in terms of precision and accuracy, costs for a surface survey platform can be even lower, and the accessibility to non-technical users higher.

This work presents a surface platform to gather bathymetric data in shallow water assembled using off-the-shelf equipment: a non-differential GNSS system, one GoPro Hero 4, and a portable echosounder (a fishfinder), all mounted on an inflatable diver's buoy and connected to a smartphone. SfM/MVS was used to process the seabed images gathered with this system, producing an orthomosaic of the seabed and the associated digital bathymetric model (DBM). Half of the echosounder points were used to improve the bathymetric reconstruction, and the remaining half was employed to assess the accuracy of the DBM. The precision of the DBMs obtained with this technique was tested in operational conditions by comparing surveys of the same area on different dates and in slightly different environmental conditions. The Python code that was developed to preprocess and postprocess the data are shared in the Supplementary Material annexed to this work.

2. Methods

The site where the platform was tested is located in the Western Mediterranean, in the Italian region of Liguria. Here, within the municipality of Finale Ligure at a location called Varigotti, lies a bay that is locally known with the name of "*Baia dei Saraceni*". The bay is characterised by the presence of a beachrock (i.e., a lithified coastal deposit, Mauz et al. [40]), formed during the last part of the Holocene [41]. The beachrock extends from the sea surface down to a 5–7 m depth (Figure 1A,B).

Figure 1. (**A**) Map of the Italian Peninsula. The star indicates the study site. Site where the test area (dashed line) is located as seen in: (**B**) orthomosaic of the area (Background image from Google Earth, 2022) and (**C**) oblique drone photo.

In the test site, the same portion of the seafloor was mapped four times on different days between 28 July and 13 August 2020. Each survey was conducted early in the morning (Table 1) with the sun at a low angle over the sea surface. On 13 August, the weather was slightly overcast, while on the other dates, it was sunny. The survey equipment consisted of a relatively large inflatable dive buoy (80 cm × 30 cm, model: Cressi Signal by Cressi Sub, Genova, Italy) dragged by an operator working with mask and snorkel (i.e., snorkelling) following a grid pattern (Figure 1A) over the seafloor. Above the sea surface, in a dry case fixed on the buoy, were positioned a Global Navigation Satellite System receiver (model: BadElf GPS Pro+, BadElf LLC, West Hartford, AZ, USA) and an Android smartphone (model: Huawei P20 Pro, Huawei Technologies Co., Ltd., Shenzen, China). Below the sea surface, attached to the buoy, is a GoPro Hero 4 Silver (GoPro Inc., San Mateo, CA, USA) in its diving case and a portable echosounder (model: Deeper Pro+, Deeper UAB, Vilnius, Lithuania). The GNSS receiver and Android phone were placed inside a waterproof kitchen container. Inside the container, one small ice brick was placed to keep the system from overheating. A simple sketch of the survey setup is shown in Figure 2.

Table 1. Summary of the results of the four surveys carried out in the test area. The timezone of the test area is UTC+2. The area surveyed refers to the area available post-clipping (see Section 2 for details).

Date	Start Time (hh:mm UTC)	Survey Duration (Minutes)	Area Surveyed (sqm)	Number of Images (% Aligned)	Orthomosaic Resolution (mm/pix)	DBM Resolution (mm/pix)	Number of Echosounder Points	Postprocessing Vertical Correction (m)
28 July 2020	07:31	21	420	1682 (88%)	1.14	2.28	336	−0.04
30 July 2020	07:16	21	437	1838 (82%)	1.05	2.1	326	0.13
7 August 2020	07:21	27	440	1812 (79%)	1.08	2.15	370	0.04
13 August 2020	06:14	21	488	1778 (100%)	1.17	2.33	388	0.05

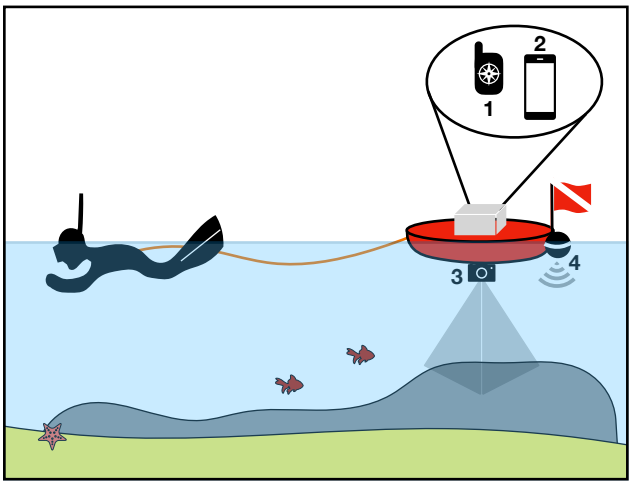

Figure 2. Field setup used in this study. An operator working in snorkelling is dragging a diver's buoy on top of which are fixed a dry case with a GNSS receiver (1) and a mobile phone (2). Fixed on the underwater part of the diver's buoy are located a GoPro camera (3) and a portable echosounder (4). See text for details. The drawing is not to scale.

2.1. Mapping Operations

To be able to follow the same workflow used in this study, the GNSS receiver should have the possibility to share its location via Bluetooth and record its track in *gpx* format. On the smartphone was installed one among the several free apps (this study used the "Bluetooth GPS" app available on the Google Play Store) that allow receiving position information via Bluetooth from an external device and streaming this position to any device connecting to the smartphone, masking the internal smartphone GNSS receiver. This is completed to ensure that the portable echosounder and the camera would receive the positioning information from the same device. Once the GNSS was receiving position information and successfully streaming it to the smartphone, one picture of the main GNSS screen (showing time and position, Figure A1) was taken by the surveyor. This is completed to be able, in postprocessing, to synchronise the pictures with the *gpx* track. Next, the echosounder was connected to its native Android application (FishDeeper app, freely available on the Google Play Store and on the Apple Store for iOS devices, Figure A1). The GoPro camera was set to collect pictures with a frequency of 2 Hz (2 pictures per second).

Once the operator reached the test site, they started to swim slowly (~1 fin stroke per second) following a grid pattern (Figure 3A) and orienting themselves using conspicuous features on the seafloor.

After the data collection, five datasets were available.

1. One photo of the screen of the GNSS receiver showing GPS time taken with the camera used for the survey
2. Photos of the seafloor taken with the same camera (12 MP, 72 PPI)
3. A *csv* file exported from the echosounder, containing position and depth information
4. A *gpx* file exported from the GNSS receiver containing the track followed by the snorkelling operator
5. A *csv* file with tidal values for the time of survey from a nearby tide gauge

In this study, tidal values were obtained from the tide gauge of Genoa (that is maintained by the government agency ISPRA—*Istituto Superiore per la Protezione e la Ricerca Ambientale*), located ~50 km NE of the study area.

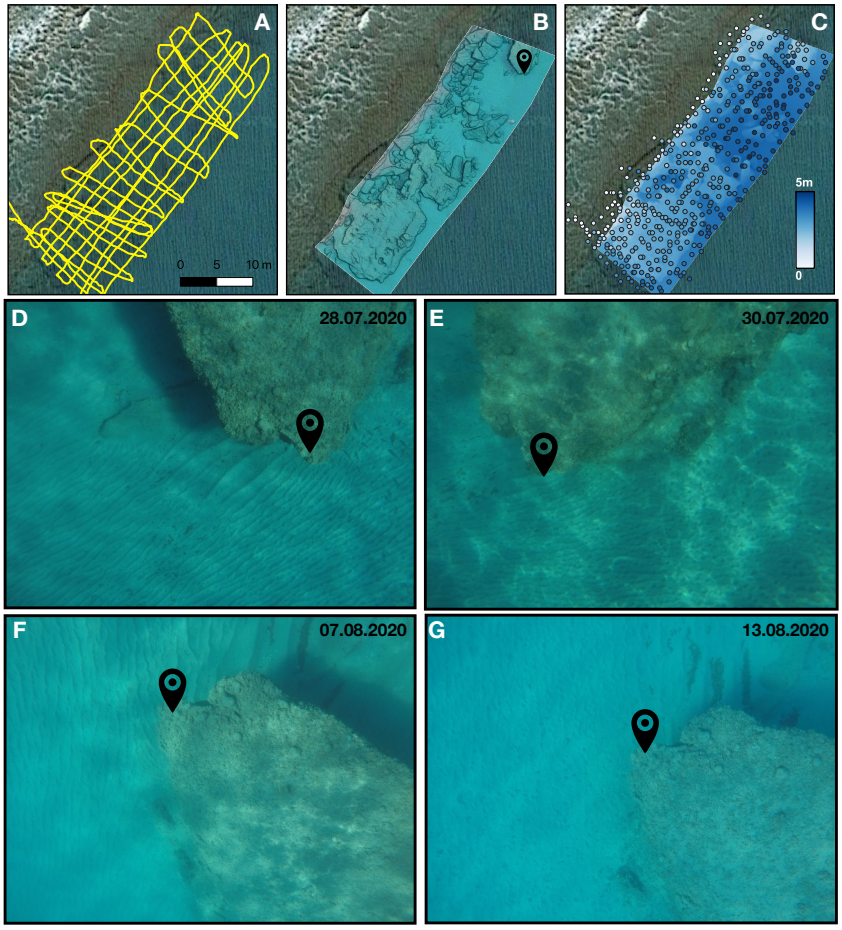

Figure 3. Example of results obtained using the workflow outlined in the main text. (**A**) grid pattern followed by the snorkelling operator. (**B**) Orthomosaic (with hillshade in the background). (**C**) Digital bathymetric model (DBM) and echosounder points. Panels A, B, and C refer to the survey performed on the 13 August 2020. The same results for all surveys are shown in Figure A2. (**D**–**G**) show an example of a picture for each survey date. The location pin (also shown in panel B) helps orient the image and place it in the reconstructed scene.

2.2. Data Preprocessing

After the data collection, a series of preprocessing steps were done via a Jupyter Notebook (written in Python) that is available in the Supplementary Materials. In the Jupyter Notebook, the timestamps of the echosounder data points are compared with the tide gauge data. Then, the bathymetric data are corrected for the tide at the moment of the survey, and the average water level during the survey is calculated.

The *Python Image Library* is then used to compare the timestamp written on the Exif metadata of each picture to the timestamps in the *gpx* file. As camera and GNSS time are never perfectly coincident, the preprocessing script allows using the photo of the screen of the GNSS receiver to adjust for any time lag between the two. The script writes a file called *"camera_coordinates.txt"* that contains:

1. **Label**. The image filename of the image.
2. **Latitude, Longitude**. The coordinates extracted from the *gpx* file.
3. **Altitude**. The average water level calculated from the tidal data.
4. **Hrz Accuracy**. The horizontal accuracy of the photo position is set to 1 m.
5. **Vrt Accuracy**. The vertical accuracy of the photo elevation is set to 0.2 m.

6. **Time difference**. The difference (in seconds) between the photo time and the *gpx* time, saved for debugging purposes (normally, this value should be 0.0 s).

2.3. SfM/MVS Processing

The photos of the seafloor were imported in the software Agisoft Metashape Professional (version 2.1.2 build 18548). The "*camera_coordinates.txt*" file was then used to add the positioning references to each camera. Agisoft Metashape was then used to align the photos, optimise the alignment, generate a point cloud, a digital elevation (bathymetric) model, and an orthomosaic. Using a PC equipped with a 127.82 GB RAM, a 13th Gen. Intel(R) Core(TM) i7-13700F CPU, and an NVIDIA GeForce RTX 4070 GPU, the processing time was between about two and three hours (Table 2). The details of each processing are reported in the Agisoft Metashape reports within the Supplementary Materials annexed to this paper. Extracts from the reports showing the processing parameters are reported in Appendix A.

Table 2. Summary of processing times and manual operations performed on the point cloud in Agisoft Metashape.

Date	Total Processing Time (hh:mm)	Point Cloud Filtering Operations
28 July 2020	02:06	Filtered out points with confidence less or equal to 1
30 July 2020	02:10	Filtered out points with confidence less or equal to 2
7 August 2020	01:52	Filtered out points with confidence less or equal to 1 Smooth point cloud: radius (m) 0.02
13 August 2020	02:59	Filtered out points with confidence less or equal to 3

The only survey for which all photos were aligned is the one of 13 August 2020. For the other projects, it was not possible to align all photos (probably due to the effect of caustics). However, the number of aligned photos was increased by resetting the alignment and re-aligning the misaligned photos. This functionality embedded in Agisoft Metashape allows you to rerun the alignment step only on the unaligned cameras, while the other cameras retain the original alignment parameters.

After the point cloud was built in Agisoft Metashape, an outer boundary was created to exclude the peripheral areas of the reconstructed scene, and such a boundary was used to clip both the DBM and the orthomosaic. Before building the DBM, the point cloud was cleaned by filtering out points with low confidence (depending on the survey, points with confidence less than 3 or less than 1 were filtered out Table 2). The DBMs and orthomosaics were exported in UTM (EPSG 32632).

It is worth noting that, while the main Agisoft Metashape parameters were kept the same throughout all surveys, the re-alignment and filtering described above were carried out to achieve the best possible DBM, free as much as possible from noise and artefacts introduced by caustics or misaligned elements in the pictures.

2.4. Postprocessing

The postprocessing was carried out with a Jupyter Notebook (written in Python), where the echosounder data was first clipped to the extent of the DBM and then split into two random subsets. One was used as a calibration dataset for the *optimize.minimize* function of the *scipy* library, which was employed to find the best vertical shift to minimise the root mean square error between the calibration echosounder points and the corresponding DBM values. The second subset was used as a validation dataset to establish the RMSE of the optimised DBM. To compare the echosounder points to the raster values of the DBM, the *rasterio* library was used, which uses a natural neighbour interpolation.

To test the precision, the geographic location (in terms of latitude and longitude) of the DBMs was co-registered to a common reference, given the low XY positional accuracy that

can be attained with a handheld GNSS working close to the sea surface (causing multi-path errors [42]). The common reference adopted was the product of the survey carried out on 13 August. Using the *georeferencer* tool in Quantum GIS (QGIS), ten ground control points were selected in correspondence with conspicuous seafloor features. Through these points, all orthomosaics were co-registered to the 13 August one using a polynomial 2 transformation. The co-registration parameters used for the orthomosaics were saved and applied to the corresponding DBMs. After co-registration, the DBMs were clipped to a common rectangular extent using QGIS and processed in Python to calculate the average and RMSE of depth differences. To carry out this comparison, each target DBM was resampled to match the base DBM (13 August) with the *rasterio* library, using bilinear resampling (i.e., interpolating pixel values based on the four nearest pixels).

3. Test Results

In the following sections are presented the results obtained in the test site. Then, the DBM depths are compared against the validation echosounder data collected contextually to each survey. This allows testing the accuracy of the survey platform. To explore its precision, the co-registered DBMs are compared to each other.

3.1. Description of Products

Four surveys at different times were carried out in the study site. Each survey lasted between 21 and 27 min and allowed mapping an area of 420–488 m^2 with 1700–1800 images per survey and a success rate in the alignment of photos ranging between 79% to 100%. The final orthomosaic resolution was always around 1.1 mm/pix, and DBM resolution was between 2.1 and 2.3 mm/pix (Table 1). For each survey, between 326 and 388 echosounder points were collected (Table 1, Figure 3C). The survey for which the alignment processing reached a success of 100% is the one carried out on 13 August, followed by the one on 28 July (88%), then those of 30 July (82%) and 7 August (79%, Table 1).

The success in the alignment process is reflected in the number of points with high or low confidence in the final point cloud calculated by Agisoft Metashape. This corresponds to the number of combined depth maps contributing to the definition of a single point. Higher percentages of points with high confidence mean that the point cloud, and hence the DBM, is more accurate (Figure 4).

As a result of the optimisation postprocessing, which included the minimisation of the RMSE via echosounder calibration points, the DBMs were shifted vertically by the amounts reported in Table 1. Overall, this shift is minimal, between 4 and 13 cm.

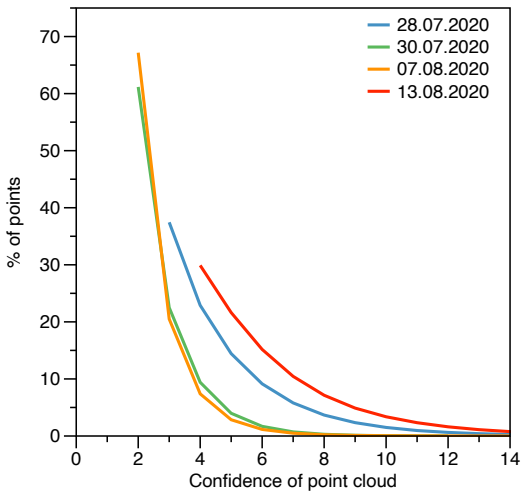

Figure 4. Percentage of points and corresponding confidence calculated by Agisoft Metashape. Note that the surveys of 28 July and 13 August have higher confidence than the other two surveys, for which fewer photos were aligned by the program.

3.2. Accuracy of Digital Bathymetric Models

By design, the bathymetric points were geolocated with the same GNSS data used to georeference the seabed photos from which the DBMs have been calculated, and both the DBM and bathymetric points are referred to the mean sea level of the Genoa tide gauge. Therefore, as the echosounder is located very close to the camera (less than 10 cm from it), 50% of the echosounder points were used to benchmark the accuracy of each DBM (the remaining 50% was used for calibration, as described in the Methods Section). Following the standard definition of "accuracy," and considering the echosounder points as the true depth values in the area, this comparison allows us to test the difference between the SfM/MVS reconstructions and the real bathymetry.

There is an overall good agreement between the value extracted from the DBMs and bathymetric points measured with the portable echosounder (Figure 5A–D), with average differences varying between 6 mm and 4 cm and RMSE between 29 and 43 cm. In terms of average, the best-performing survey is the one carried out on 13 August (Figure 5D), while the lowest RMSE is attained by the survey completed on 30 July (Figure 5B). Exploring the depth distribution of RMSE, there is no clear relationship between depth and RMSE. Depending on the survey, depths showing higher RMSEs are either deeper or shallower ones, with average depths showing RMSEs closer to the overall RMSE (Figure A3).

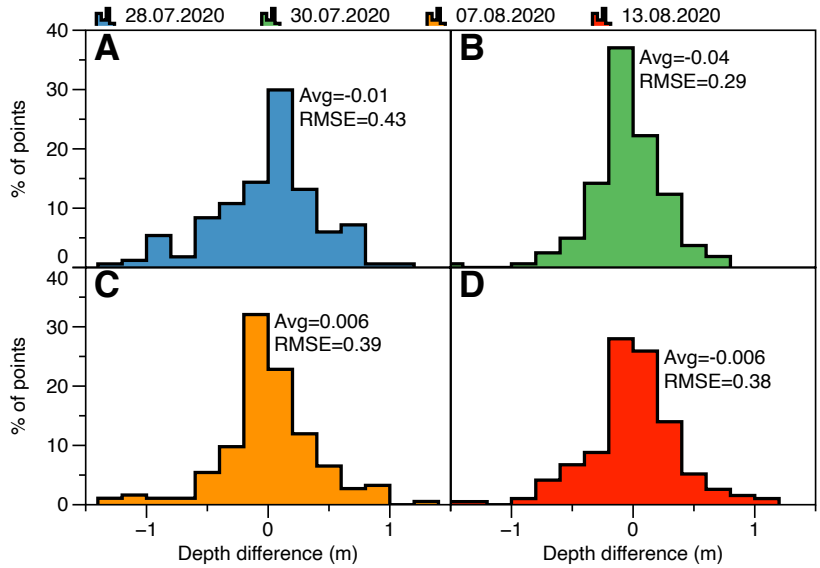

Figure 5. Histograms showing the depth differences between DBM depths and control echosounder points (that represent the accuracy of each DBM), with average difference and RMSE for each survey date (panels **A**–**D**). For a plot of echosounder depths versus DBM depths, see Figure A4.

3.3. Precision of Orthomosaics and Digital Bathymetric Models

The orthomosaics were obtained via the SfM/MVS processing with photos georeferenced through a non-differential GNSS receiver. This positioning system has an accuracy that allows geographic positioning with, at best, metric errors in optimal satellite reception conditions. Therefore, there is a low positioning accuracy that is reflected in a positional shift of orthomosaics and DBMs from different surveys. To test the precision of the DBMs, i.e., how much a DBM from a survey on a given date differs from the other DBMs, co-registered DBMs are compared to each other, calculating the average and RMSE of the differences between each pair of DBMs.

Overall, the average differences between DBMs are between 1 mm and 13 cm (Table 3), while the RMSE is between 7 and 19 cm (Table 3). The mapped differences between DBMs are shown in Figure A5, which are also plotted as histograms in Figure A6.

Table 3. Average and RMSE of the differences between DBMs surveyed at different dates.

Base DBM	Target DBM	Average Difference (m)	RMSE (m)
13/08	30/07	0.14	0.19
13/08	28/07	−0.001	0.06
28/07	30/07	0.15	0.19
07/08	30/07	0.10	0.17
07/08	13/08	−0.04	0.14
07/08	28/07	−0.04	0.13

4. Discussion

The platform presented and tested in this study allows obtaining orthomosaics and digital bathymetric models of shallow-water areas using off-the-shelf software and hardware and with very limited effort and cost. The average survey efficiency (from the data reported in Table 1) is ~20 m^2 per min, which translates to 0.12 hectares per h. The average mapping efficiency (which also includes the processing time needed for Agisoft Metashape to produce orthomosaics and DBMs shown in Table 2) is ~3.3 m^2 per min (~0.02 hectares per h).

A key aspect of the equipment choice for this study was the ease of use. The aim was to avoid a setup that may need professional training, such as an RTK GNSS system. Another key aspect taken into account in the development of the platform is its high portability: thanks to the fact that the selected diving buoy is inflatable, the entire platform can be transported in a small backpack.

4.1. Cost of the Platform

The platform presented in this study was designed to achieve the best results with the lowest possible costs (Table 4). Priority was given to off-the-shelf, low-cost equipment, which can be bought either in the used market or obtained at a fraction of the costs with respect to the latest models. Overall, the cost of the survey platform employed is ~885 €.

Including the costs of Agisoft Metashape and the workstation used to process the data, there is an additional cost of 3110 €. However, taking into account that the entire processing time for this work was 9 h and 21 min (Table 2), the entire processing (under a non-commercial clause) could have been run entirely on the Agisoft Metashape Cloud (20 free processing hours per month), therefore avoiding the cost of the workstation.

Overall, the cost of the platform presented in this work is significantly lower even than the already low-cost POSEIDON platform [37] (~1500 $, ~1400 €) and has a fraction of the cost of more elaborate systems employing unoccupied or towed surface vehicles with multiple cameras and/or RTK GNSS positioning, e.g., [43].

Table 4. Costs of the equipment employed in this study. * Available in the used market. ** Discontinued price is for a new model (Bad Elf Flex Mini). *** Approximate cost of educational license. **** If processing is less than 20 h per month, it can be carried out on the Agisoft Metashape Cloud for free.

Item	Model	2024 Cost (€)
Android phone	HuaweiP20 Pro	150
Echosounder	Deeper Pro	180
Action camera	GoPro Hero 4 Silver	100 *
Bluetooth GNSS	BadElf GPS Pro+ **	460
Diving buoy	Cressi Signal	80
Other tools	Waterproof box	10
Other tools	Ice brick	5
Total		**885**
SfM/MVS software	Agisoft Metashape ***	510
Workstation ****		2600
Total		**3110**

4.2. Resolution of Final Products

The resolution of the resulting orthomosaics and DBMs is very high (respectively, on average, 1.1 mm/pixel and 2.2 mm/pixel) thanks to the low camera-to-seafloor distance and the high overlap that was achieved swimming slowly while dragging the diver's buoy. Such high-resolution final products may be suitable for ecological, geological, or archeological studies with the goals of obtaining precise mapping of the seafloor and/or recognising small-scale topographic features. The depth limits of the methodology were not tested; however, it is worth pointing out that at higher depths the technique is limited by water turbidity and, obviously, light absorption. In coral reef areas, or in areas with clear water, this method should allow mapping up to several metres depth. Towards the sea surface, the technique is limited by the proximity of the seabed to the camera: the closer the seabed, the smaller the camera footprint (see Figure 4a in [37]) (for an example), therefore, the slower the diver should swim to have a good overlap. Even with small wave ripples, achieving a good overlap might prove impossible without a second camera [37]. It follows logically that the method proposed in this work may give poor results at depths shallower than −2 m.

Understanding the potential effect of caustics is important to achieve optimal alignment of photos in the SfM/MVS processing [22]. In the attempt to avoid caustics, the surveys described in this work were performed early in the morning, with the sun low on the sea surface. However, there is still some degree of caustic reflection on the seafloor (compare images in Figure 3D–F). The only day where the weather was slightly overcast is the only one where 100% of the collected pictures were correctly processed (Table 1), albeit there was a slightly lower visibility (Figure 3G). However, despite caustics (that can be minimised by the choice of survey conditions), SfM/MVS algorithms produced a reliable outcome. The reliability of the reconstruction can be assessed by cross-checking the confidence of points calculated by Agisoft Metashape for the point clouds: if the confidence curve falls below the ones obtained in this work (Figure 4), images would need to be pre-processed to reduce the effect of caustics [21,22].

Another relevant point to consider when employing the technique described in this study is the nature of the substrate. In the test area, the scene contains many different features due to the fragmentation of the beachrock providing many solid potential tiepoints to SfM/MVS. Therefore, the method presented here will perform better in coral reefs and other diverse substrates (including areas with man-made underwater constructions) than on sandy or vegetated bottoms, with plants moving under the influence of currents and waves.

4.3. Accuracy and Precision of DBMs

For which concerns the accuracy and precision of the DBMs, the average depth accuracy is in the range of a few centimetres, which is in line with most studies employing underwater SfM/MVS to reconstruct bathymetry (Table 5). However, the accuracy RMSE is one order of magnitude higher in this work with respect to published ones, with the exception of the RMSE obtained by Ventura et al. [33], who compared the DBMs obtained with SfM/MVS against transects of a multi-beam survey of the same area. Most of the other works shown in Table 5 assess the depth accuracy against single control points, which might limit the statistical significance of the calculated standard deviation or RMSE.

For which concerns depth precision (that correlates with the repeatability of the results obtained by the technique), the average precision is between 1 mm and 14 cm, with an RMSE between 6 and 19 cm (Table 5). The lowest depth differences (both in terms of average and RMSE) are calculated between the DBMs carried out on 28 July and that carried out on 13 August, which are the ones with the higher percentage of pictures processed (Table 1) and the best ratios of point confidence (Figure 4). It follows that checking these two parameters (together with the presence of caustics in the pictures) may help assess the quality of the final results.

Table 5. Comparison between average and standard deviation (or *RMSE*) obtained by different works employing SfM/MVS to map the seafloor. * indicates that the study reports RMSE; ** indicates RMSE given as XYZ

Reference	Technique	Average Accuracy (m)	RMSE or StDev Accuracy (m)	Average Precision (m)	RMSE or StDev Precision (m)
This work *	SfM/MVS from surface platform (one camera) with no ground control points (GCPs), non-differential GNSS positioning and fishfinder echosounder depth control.	0.01 0.04 0.006 −0.006	0.43 0.29 0.39 0.38	0.14 −0.001 0.15 0.10 −0.04 −0.04	0.19 0.06 0.19 0.17 0.14 0.13
Lo et al. [44] *	SfM/MVS from surface platform connected with RTK GNSS. Accuracy assessed against 5 CPs placed on the seafloor.	-	0.003 0.002 0.003 0.002 0.003	-	-
Hatcher et al. [38]	SfM/MVS from surface platform (five cameras) with no GCPs and RTK GNSS camera positioning. Water depth accuracy tested against fixed plates on the seafloor. Precision tested with overlapping DBMs taken during two surveys.	0.004	0.018	0.001	0.01
Jaud et al. [37]	SfM/MVS from surface platform (two cameras) with no GCPs and RTK GNSS camera positioning. Accuracy tested against test on-land SfM at high tide and precision tested on repeated surveys.	0.052	0.046	−0.017 0.013 0.030	0.063 0.062 0.078
Ventura et al. [33] *	SfM/MVS from diver operator with GCPs measured with RTK GNSS, accuracy tested on check points (CPs) and multibeam bathymetry (transects).	n/a 0.18	0.016 0.3	-	-
Hatcher et al. [43]	SfM/MVS from surface platform (five cameras) with no GCPs and RTK GNSS camera positioning. Water depth accuracy tested against two fixed plates on the seafloor. Precision tested with a subset area of the DBM taken during two surveys.	~0.03	-	0.008	0.003
Nocerino et al. [35] *	Diver-operated camera (different cameras and different distance of acquisition) with network of GCPs (used for referencing the point cloud) and CPs (used to assess precision) measured with RTK GNSS.	-	-	-	0.002 0.005
Abadie et al. [39] **	SfM/MVS from surface platform (one camera) with accuracy tested against multibeam echosounder.	-	-	-	0.48 0.51

Overall, for which concerns precision, these results are at the lower end of those reported in literature for similar studies (Table 5). This is not surprising, given that these works employ RTK GNSS positioning of the camera or use in the SfM/MVS processing ground control points (GCPs) placed on the seafloor and measured with RTK GNSS. Avoiding these high-accuracy positioning techniques for ease of use and portability has the disadvantage that precision is decreased. Another key factor that might contribute to the lower precision of the surveys presented in this work compared to other studies is the complex nature of the beachrock mapped in this work, with crevices, vertical surfaces, and overhangs that make the SfM/MVS processing more uncertain [43]. In this study, these areas are often showing as those with higher accuracy errors (Figure A5).

4.4. Future Improvements

For which concerns improvements to the survey platform presented here, higher positional accuracy can be attained substituting the handheld GNSS with a differential GNSS system, as in the POSEIDON platform [37]. However, this would require either the presence of a GNSS base station nearby maintained by state or regional authorities or a second base station broadcasting precise positions, adding to the overall costs and ease of operation of the system. Adding an RTK GNSS system would also cause problems with the positioning of the echosounder data, as the low-cost echosounder employed in this work cannot be, by design, connected to the positioning stream of an RTK GNSS.

Another improvement that may help reduce the relatively large accuracy RMSEs found in this work is the improvement of the base images, either with a camera with better resolution than the GoPro Hero 4 Silver used in this work (at higher costs) or by enhancing the images via image enhancement techniques (e.g., Wang et al. [45])

5. Conclusions

This work shows a simple, low-cost, highly portable platform that allows gathering sequential photos of shallow-water sites and surveying contextually echosounder depth values that are then used to calibrate and validate the digital bathymetric models obtained via SfM/MVS methods. The survey platform can be operated by a single snorkelling operator and fits in a small backpack, as it is installed on an inflatable diving buoy.

The data analysis involves minimal preprocessing and postprocessing, which are summarised in two Python Jupyter notebooks (available in the Supplementary Material annexed to this work). To process the data, tidal data from a tide gauge are needed. In the absence of such data, one can rely either on an ad-hoc pressure transducer [46] or on tidal models (e.g., the FES 2014 global model, [47]).

The DBMs obtained with the platform presented in this work have a centimetric average accuracy and precision (with accuracy RMSEs between 30 and 40 cm and precision RMSEs in the order of 6–20 cm). In light of these data, the platform performs worse than other similar tools proposed in the literature (Table 5). However, it is the only one allowing the gathering of, contextually to the photos, echosounder data for a survey-specific accuracy assessment. This gives the opportunity to evaluate, with the data collected in a single survey, the accuracy of the final products.

As reported in other studies [22], caustics remain a problematic issue in reconstructing shallow-water areas through SfM/MVS, decreasing the number of processed images and increasing the bathymetric errors. For this reason, the choice of the time and weather for the survey is crucial to maximise the results of the SfM/MVS processing and avoid complex postprocessing to remove caustics (which is still in the experimental phase [22]).

Overall, the bathymetric data and the orthomosaics obtained with the platform employed here have a very high resolution and a good accuracy, and could represent a valuable alternative to acoustic systems for conducting ecological, geological, archeological, and geomorphological studies in shallow coastal waters. As the system is composed of off-the-shelf (and relatively inexpensive) instruments, it can be assembled with ease also in contexts where financial resources could be limited, e.g., in developing countries. Its low cost and ease of operation make it ideal for rapid mapping applications, including activities involving citizen scientists doing shallow-water mapping, such as those described by Raoult et al. [48], allowing for obtaining independent depth accuracy contextually to DBMs and orthomosaics.

Supplementary Materials: The following supporting information can be downloaded at: https://www.mdpi.com/article/10.3390/rs16224321/s1. The Supplementary Material for this article is available on Zenodo as Casella and Rovere [49]. The repository contains all the data acquired in this work and the code used for the analyses described in the manuscript. The code in the Supplementary Material has been improved with the assistance of ChatGPT, which provided guidance on optimisation, debugging, and documentation to enhance clarity and functionality. All the code has been reviewed and supervised by humans to ensure consistency and correctness. Supplementary figures are shown in Appendix B, and extracts of the Agisoft Metashape reports are shown in Appendix A.

Author Contributions: Conceptualization, E.C. and A.R.; methodology, E.C. and A.R.; software, A.R.; formal analysis, E.C., A.R. and G.S.; investigation, E.C., A.R. and G.S.; writing—original draft preparation, E.C., A.R. and G.S.; writing—review and editing, E.C., A.R. and G.S. All authors have read and agreed to the published version of the manuscript.

Funding: This research received internal funding from Ca' Foscari University of Venice, from the University of Bari and from the University of Bremen.

Data Availability Statement: All data and code described in this paper is available in Zenodo as Casella and Rovere [49].

Conflicts of Interest: The authors declare no conflicts of interest.

Appendix A. Agisoft Metashape Processing Reports

This appendix contains parts of the Agisoft Metashape reports showing the processing parameters. To download the raw data, Jupyter Notebooks and python scripts mentioned in the text, the reader is referred to

Casella and Rovere [49] (https://doi.org/10.5281/zenodo.14014224 (accessed on 8 November 2024).

Appendix A.1. 28 July 2020

Processing Parameters

General	
Images	1643
Aligned images	1447
Shapes	
Polygon	1
Coordinate system	WGS 84 (EPSG::4326)
Coordinate system	WGS 84 (EPSG::4326)
Rotation angles	Yaw, Pitch, Roll
Tie Points	
Points	1,036,888 of 1,273,454
RMS reprojection error	0.634541 (1.8364 pix)
Max reprojection error	2.93367 (89.0802 pix)
Mean key point size	2.93435 pix
Point colors	3 bands, uint8
Key points	No
Average tie point multiplicity	2.73863
Alignment parameters	
Accuracy	Highest
Generic preselection	Yes
Reference preselection	Source
Key point limit	40,000
Key point limit per Mpx	1,000
Tie point limit	4,000
Exclude stationary tie points	Yes
Guided image matching	No
Adaptive camera model fitting	No
Matching time	6 minutes 33 seconds
Matching memory usage	696.84 MB
Alignment time	15 minutes 56 seconds
Alignment memory usage	631.00 MB
Optimization parameters	
Parameters	f, cx, cy, k1-k3, p1, p2
Adaptive camera model fitting	No
Exclude corners	No
Optimization time	23 seconds
Date created	2024:09:05 21:19:27
Software version	2.1.2.18548
File size	80.80 MB
Depth Maps	
Count	1443
Depth maps generation parameters	
Quality	High
Filtering mode	Mild
Max neighbors	16
Processing time	21 minutes 45 seconds
Memory usage	2.80 GB
Date created	2024:09:06 16:10:28
Software version	2.1.2.18548
File size	2.50 GB
Point Cloud	

Points	63,182,228
Point attributes	
Color	3 bands, uint8
Normal	
Confidence	3 - 37
Point classes	
Created (never classified)	63,182,228
Depth maps generation parameters	
Quality	High
Filtering mode	Mild
Max neighbors	16
Processing time	21 minutes 45 seconds
Memory usage	2.80 GB
Point cloud generation parameters	
Processing time	47 minutes 15 seconds
Memory usage	13.96 GB
Date created	2024:09:06 16:57:44
Software version	2.1.2.18548
File size	3.22 GB
DEM	
Size	13,512 x 18,521
Resolution	2.28 mm/pix
Coordinate system	WGS 84 (EPSG::4326)
Reconstruction parameters	
Source data	Point cloud
Interpolation	Enabled
Processing time	49 seconds
Memory usage	308.50 MB
Date created	2024:09:06 22:47:28
Software version	2.1.2.18548
File size	587.51 MB
Orthomosaic	
Size	27,024 x 37,042
Resolution	1.14 mm/pix
Coordinate system	WGS 84 (EPSG::4326)
Colors	3 bands, uint8
Reconstruction parameters	
Blending mode	Mosaic
Surface	DEM
Enable hole filling	Yes
Enable ghosting filter	No
Processing time	11 minutes 51 seconds
Memory usage	1.74 GB
Date created	2024:09:07 20:15:52
Software version	2.1.2.18548
File size	5.82 GB
System	
Software name	Agisoft Metashape Professional
Software version	2.1.2 build 18548
OS	Windows 64 bit
RAM	127.82 GB
CPU	13th Gen Intel(R) Core(TM) i7-13700F
GPU(s)	NVIDIA GeForce RTX 4070

Appendix A.2. 30 July 2020

Processing Parameters

General	
Images	1834
Aligned images	1503
Shapes	
Polygon	1
Coordinate system	WGS 84 (EPSG::4326)
Coordinate system	WGS 84 (EPSG::4326)
Rotation angles	Yaw, Pitch, Roll
Tie Points	
Points	1,186,500 of 1,421,789
RMS reprojection error	0.754614 (3.18913 pix)
Max reprojection error	2.36995 (115.603 pix)
Mean key point size	4.31051 pix
Point colors	3 bands, uint8
Key points	No
Average tie point multiplicity	2.87943
Alignment parameters	
Accuracy	High
Generic preselection	Yes
Reference preselection	Source
Key point limit	40,000
Key point limit per Mpx	1,000
Tie point limit	4,000
Exclude stationary tie points	Yes
Guided image matching	No
Adaptive camera model fitting	No
Matching time	5 minutes 27 seconds
Matching memory usage	479.77 MB
Alignment time	20 minutes 53 seconds
Alignment memory usage	587.77 MB
Date created	2024:09:06 09:34:34
Software version	2.1.2.18548
File size	93.93 MB
Depth Maps	
Count	1492
Depth maps generation parameters	
Quality	High
Filtering mode	Mild
Max neighbors	16
Processing time	21 minutes 48 seconds
Memory usage	3.10 GB
Date created	2024:09:06 20:51:32
Software version	2.1.2.18548
File size	1.55 GB
Point Cloud	
Points	95,165,878
Point attributes	
Color	3 bands, uint8
Normal	
Confidence	2 - 22

Point classes	
Created (never classified)	95,165,878
Depth maps generation parameters	
Quality	High
Filtering mode	Mild
Max neighbors	16
Processing time	21 minutes 48 seconds
Memory usage	3.10 GB
Point cloud generation parameters	
Processing time	28 minutes 50 seconds
Memory usage	12.95 GB
Date created	2024:09:06 21:20:23
Software version	2.1.2.18548
File size	3.69 GB
DEM	
Size	16,821 x 20,841
Resolution	2.1 mm/pix
Coordinate system	WGS 84 (EPSG::4326)
Reconstruction parameters	
Source data	Point cloud
Interpolation	Enabled
Processing time	1 minutes 5 seconds
Memory usage	312.07 MB
Date created	2024:09:06 22:49:22
Software version	2.1.2.18548
File size	865.65 MB
Orthomosaic	
Size	33,642 x 41,682
Resolution	1.05 mm/pix
Coordinate system	WGS 84 (EPSG::4326)
Colors	3 bands, uint8
Reconstruction parameters	
Blending mode	Mosaic
Surface	DEM
Enable hole filling	Yes
Enable ghosting filter	No
Processing time	31 minutes 7 seconds
Memory usage	2.44 GB
Date created	2024:09:07 12:22:49
Software version	2.1.2.18548
File size	6.89 GB
System	
Software name	Agisoft Metashape Professional
Software version	2.1.2 build 18548
OS	Windows 64 bit
RAM	127.82 GB
CPU	13th Gen Intel(R) Core(TM) i7-13700F
GPU(s)	NVIDIA GeForce RTX 4070

Appendix A.3. 7 August 2020

Processing Parameters

General	
Images	1813
Aligned images	1427
Shapes	
Polygon	1
Coordinate system	WGS 84 (EPSG::4326)
Coordinate system	WGS 84 (EPSG::4326)
Rotation angles	Yaw, Pitch, Roll
Tie Points	
Points	574,332 of 717,725
RMS reprojection error	0.578839 (2.57284 pix)
Max reprojection error	2.81131 (93.5717 pix)
Mean key point size	4.17367 pix
Point colors	3 bands, uint8
Key points	No
Average tie point multiplicity	2.5661
Alignment parameters	
Accuracy	Highest
Generic preselection	Yes
Reference preselection	Source
Key point limit	40,000
Key point limit per Mpx	1,000
Tie point limit	4,000
Exclude stationary tie points	Yes
Guided image matching	No
Adaptive camera model fitting	No
Matching time	19 minutes 38 seconds
Matching memory usage	661.81 MB
Alignment time	9 minutes 18 seconds
Alignment memory usage	608.26 MB
Optimization parameters	
Parameters	f, cx, cy, k1-k3, p1, p2
Adaptive camera model fitting	No
Exclude corners	No
Optimization time	8 seconds
Date created	2024:09:05 15:51:12
Software version	2.1.2.18358
File size	43.53 MB
Depth Maps	
Count	1393
Depth maps generation parameters	
Quality	High
Filtering mode	Mild
Max neighbors	16
Processing time	18 minutes 52 seconds
Memory usage	2.23 GB
Date created	2024:09:06 15:00:46
Software version	2.1.2.18548
File size	1.37 GB
Point Cloud	

Points	84,227,696
Coordinate precision	0.538 mm
Point attributes	
Color	3 bands, uint8
Normal	
Confidence	2 - 25
Point classes	
Created (never classified)	84,227,696
Depth maps generation parameters	
Quality	High
Filtering mode	Mild
Max neighbors	16
Processing time	18 minutes 52 seconds
Memory usage	2.23 GB
Point cloud generation parameters	
Processing time	26 minutes 24 seconds
Memory usage	15.51 GB
Date created	2024:09:06 15:27:11
Software version	2.1.2.18548
File size	1.28 GB
DEM	
Size	16,363 x 21,237
Resolution	2.15 mm/pix
Coordinate system	WGS 84 (EPSG::4326)
Reconstruction parameters	
Source data	Point cloud
Interpolation	Enabled
Processing time	1 minutes 1 seconds
Memory usage	313.04 MB
Date created	2024:09:06 22:46:13
Software version	2.1.2.18548
File size	945.77 MB
Orthomosaic	
Size	32,725 x 42,474
Resolution	1.08 mm/pix
Coordinate system	WGS 84 (EPSG::4326)
Colors	3 bands, uint8
Reconstruction parameters	
Blending mode	Mosaic
Surface	DEM
Enable hole filling	Yes
Enable ghosting filter	No
Processing time	19 minutes 27 seconds
Memory usage	2.90 GB
Date created	2024:09:07 22:44:13
Software version	2.1.2.18548
File size	6.94 GB
System	
Software name	Agisoft Metashape Professional
Software version	2.1.2 build 18548
OS	Windows 64 bit
RAM	127.82 GB
CPU	13th Gen Intel(R) Core(TM) i7-13700F
GPU(s)	NVIDIA GeForce RTX 4070

Appendix A.4. 13 August 2020

Processing Parameters

General	
Images	1778
Aligned images	1778
Shapes	
Polygon	1
Coordinate system	WGS 84 (EPSG::4326)
Coordinate system	WGS 84 (EPSG::4326)
Rotation angles	Yaw, Pitch, Roll
Tie Points	
Points	1,615,490 of 1,822,692
RMS reprojection error	0.691752 (4.85056 pix)
Max reprojection error	2.1087 (135.458 pix)
Mean key point size	6.99368 pix
Point colors	3 bands, uint8
Key points	No
Average tie point multiplicity	4.03332
Alignment parameters	
Accuracy	High
Generic preselection	Yes
Reference preselection	Source
Key point limit	40,000
Key point limit per Mpx	1,000
Tie point limit	4,000
Exclude stationary tie points	Yes
Guided image matching	No
Adaptive camera model fitting	No
Matching time	7 minutes 40 seconds
Matching memory usage	1.43 GB
Alignment time	19 minutes 0 seconds
Alignment memory usage	1.90 GB
Date created	2024:09:06 11:21:09
Software version	2.1.2.18548
File size	154.60 MB
Depth Maps	
Count	1778
Depth maps generation parameters	
Quality	High
Filtering mode	Mild
Max neighbors	16
Processing time	34 minutes 13 seconds
Memory usage	3.60 GB
Date created	2024:09:06 12:18:44
Software version	2.1.2.18548
File size	2.61 GB
Point Cloud	
Points	66,968,123
Point attributes	
Color	3 bands, uint8
Normal	
Confidence	4 - 44

Point classes	
Created (never classified)	66,968,123
Depth maps generation parameters	
Quality	High
Filtering mode	Mild
Max neighbors	16
Processing time	34 minutes 13 seconds
Memory usage	3.60 GB
Point cloud generation parameters	
Processing time	59 minutes 40 seconds
Memory usage	12.07 GB
Date created	2024:09:06 13:18:25
Software version	2.1.2.18548
File size	3.41 GB
DEM	
Size	15,761 x 18,437
Resolution	2.33 mm/pix
Coordinate system	WGS 84 (EPSG::4326)
Reconstruction parameters	
Source data	Point cloud
Interpolation	Enabled
Processing time	58 seconds
Memory usage	307.93 MB
Date created	2024:09:06 22:44:45
Software version	2.1.2.18548
File size	705.74 MB
Orthomosaic	
Size	31,522 x 36,873
Resolution	1.17 mm/pix
Coordinate system	WGS 84 (EPSG::4326)
Colors	3 bands, uint8
Reconstruction parameters	
Blending mode	Mosaic
Surface	DEM
Enable hole filling	Yes
Enable ghosting filter	No
Processing time	24 minutes 11 seconds
Memory usage	1.43 GB
Date created	2024:09:08 10:22:46
Software version	2.1.2.18548
File size	5.63 GB
System	
Software name	Agisoft Metashape Professional
Software version	2.1.2 build 18548
OS	Windows 64 bit
RAM	127.82 GB
CPU	13th Gen Intel(R) Core(TM) i7-13700F
GPU(s)	NVIDIA GeForce RTX 4070

Appendix B. Supplementary Figures

This appendix contains the supplementary figures mentioned in the text.

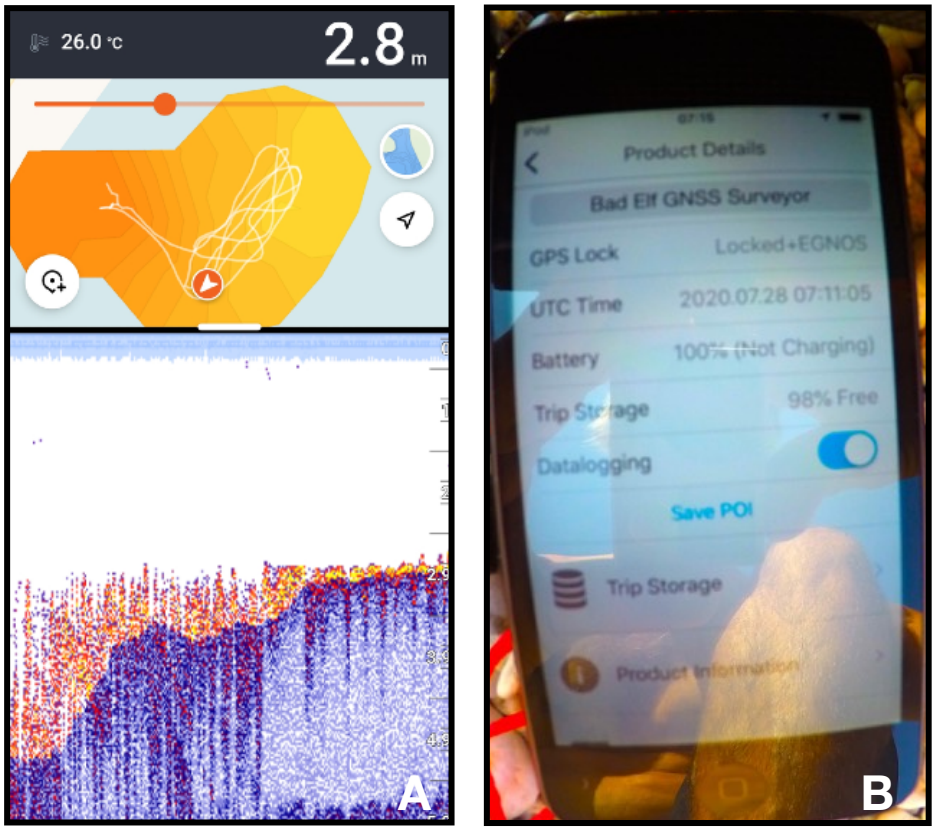

Figure A1. (**A**) Screenshot of the echosounder during data collection. The upper part shows the map location, while the lower part shows the sonogram surveyed by the echosounder. (**B**) Picture of the GNSS screen. This data is needed to syncronise the pictures taken with the GoPro camera with GNSS time.

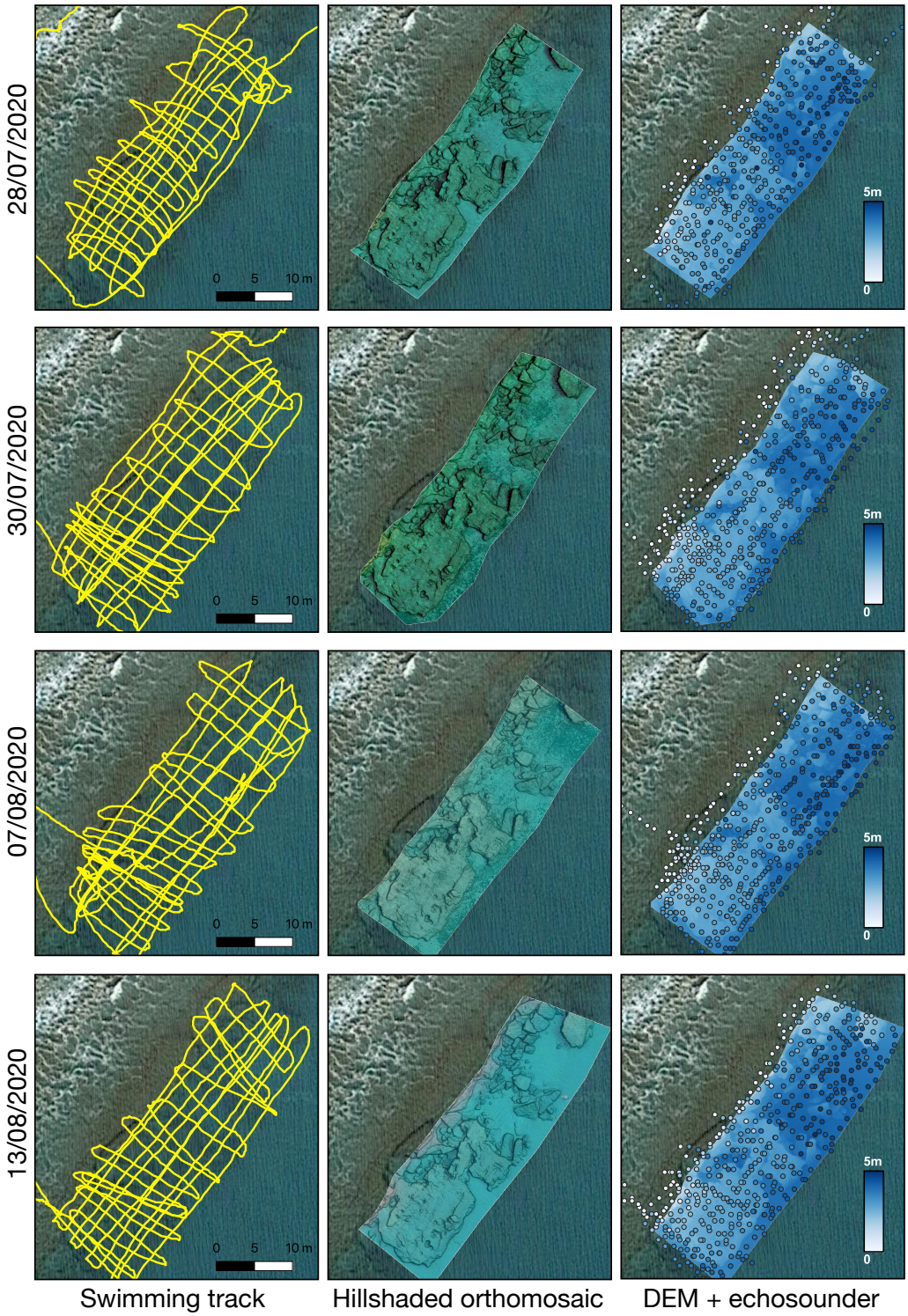

Figure A2. Same as in Figure 3, but for all survey dates. The orthomosaics and DBMs shown here are not aligned to the 13 August one.

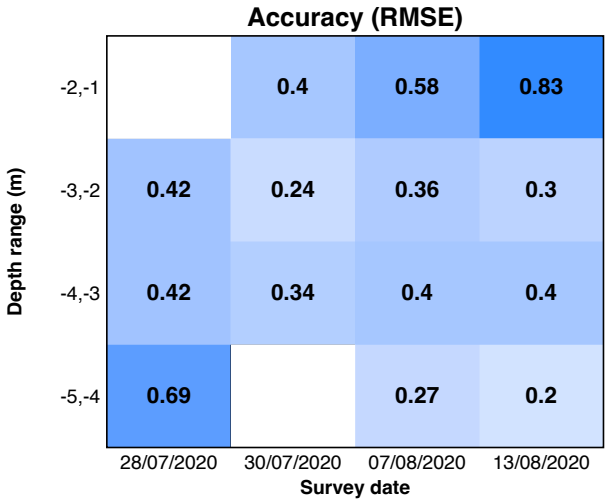

Figure A3. Heatmap showing the RMSE between echosounder control points and DBM depths divided by survey date and depth bin. Darker blue colors represent higher RMSE.

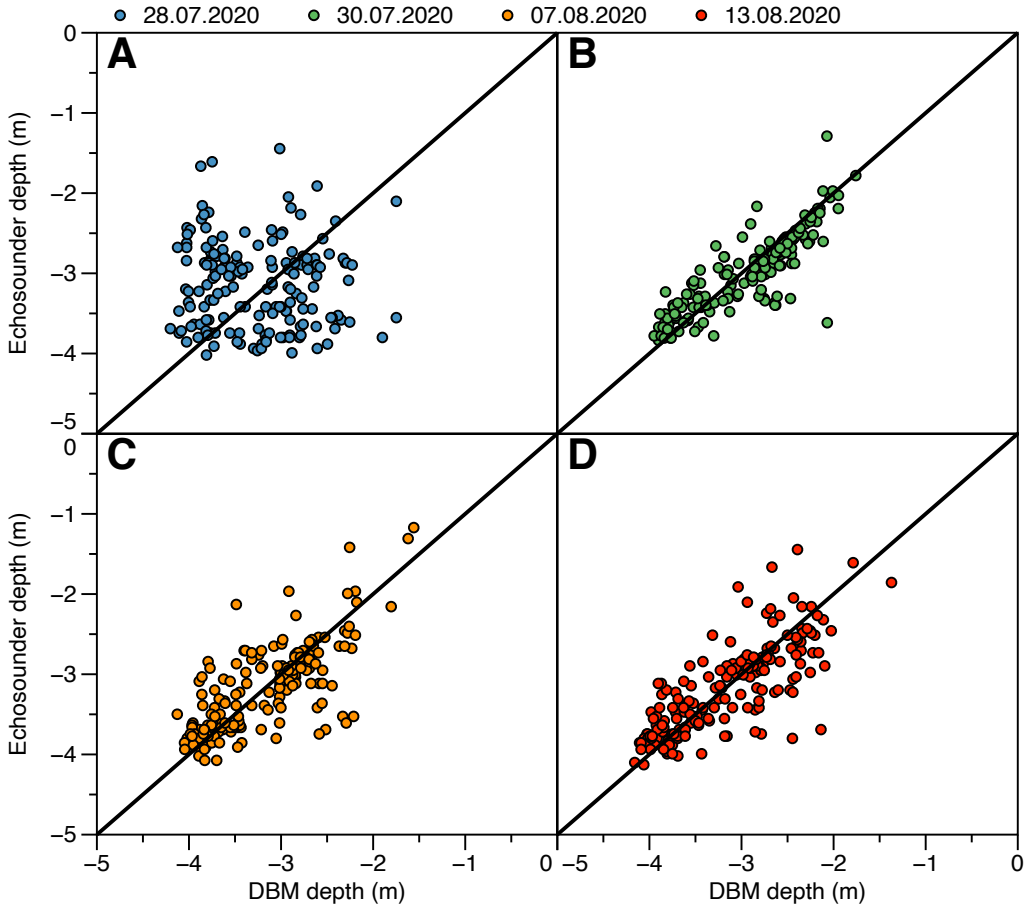

Figure A4. Scatterplots of DBM depths (x-axis) versus echosounder points depth (y-axis) for each survey date (panels **A**–**D**).

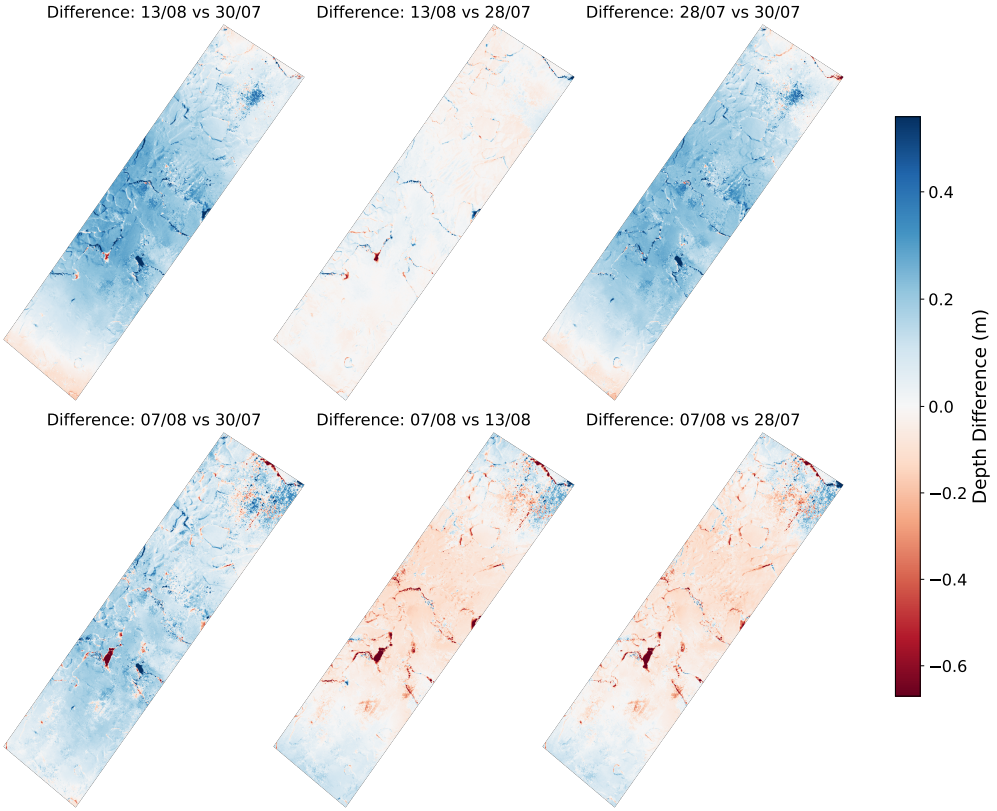

Figure A5. Maps of the differences between DBMs from surveys performed on different dates.

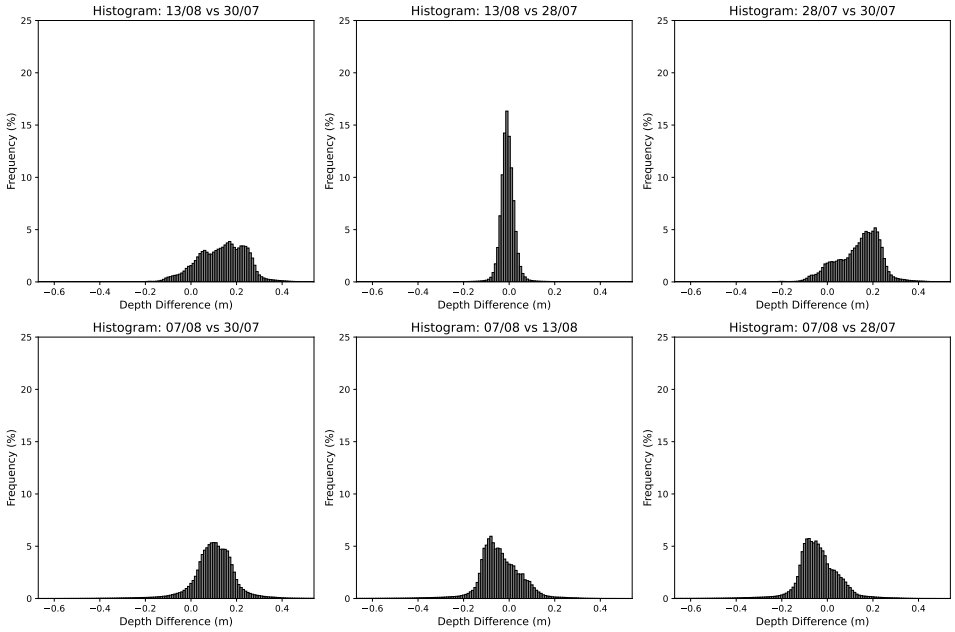

Figure A6. Histograms showing the differences between DBMs from surveys performed on different dates.

References

1. Makowski, C.; Finkl, C.W. History of modern seafloor mapping. In *Seafloor Mapping Along Continental Shelves: Research and Techniques for Visualizing Benthic Environments*; Springer: Cham, Switzerland, 2016; pp. 3–49.
2. Hughes Clarke, J.E. Multibeam Echosounders. In *Submarine Geomorphology*; Micallef, A., Krastel, S., Savini, A., Eds.; Springer International Publishing: Cham, Switzerland, 2018; pp. 25–41. [CrossRef]

3. Lurton, X. Swath bathymetry using phase difference: Theoretical analysis of acoustical measurement precision. *IEEE J. Ocean. Eng.* **2000**, *25*, 351–363. [CrossRef]
4. Liu, J.; Pang, Y.; Yan, L.; Zhu, H. An Image Quality Improvement Method in Side-Scan Sonar Based on Deconvolution. *Remote Sens.* **2023**, *15*, 4908. [CrossRef]
5. Rizzo, A.; De Giosa, F.; Donadio, C.; Scardino, G.; Scicchitano, G.; Terracciano, S.; Mastronuzzi, G. Morpho-bathymetric acoustic surveys as a tool for mapping traces of anthropogenic activities on the seafloor: The case study of the Taranto area, southern Italy. *Mar. Pollut. Bull.* **2022**, *185*, 114314. [CrossRef] [PubMed]
6. Leblond, I.; Bertholom, A.; Delumeau, I. Sidescan sonar mosaicing improvements using a tracking algorithm combining forward looking sonar images and ship heading oscillations. *Proc. Mtgs. Acoust.* **2021**, *44*, 070012.
7. Harris, D.L.; Webster, J.M.; Vila-Concejo, A.; Duce, S.; Leon, J.X.; Hacker, J. Defining multi-scale surface roughness of a coral reef using a high-resolution LiDAR digital elevation model. *Geomorphology* **2023**, *439*, 108852. [CrossRef]
8. Giordano, F.; Mattei, G.; Parente, C.; Peluso, F.; Santamaria, R. Integrating Sensors into a Marine Drone for Bathymetric 3D Surveys in Shallow Waters. *Sensors* **2015**, *16*, 41. [CrossRef]
9. Sotelo-Torres, F.; Alvarez, L.V.; Roberts, R.C. An Unmanned Surface Vehicle (USV): Development of an Autonomous Boat with a Sensor Integration System for Bathymetric Surveys. *Sensors* **2023**, *23*, 4420. [CrossRef]
10. Collin, A.; Ramambason, C.; Pastol, Y.; Casella, E.; Rovere, A.; Thiault, L.; Espiau, B.; Siu, G.; Lerouvreur, F.; Nakamura, N.; et al. Very high resolution mapping of coral reef state using airborne bathymetric LiDAR surface-intensity and drone imagery. *Int. J. Remote. Sens.* **2018**, *39*, 5676–5688. [CrossRef]
11. Ma, Y.; Xu, N.; Liu, Z.; Yang, B.; Yang, F.; Wang, X.H.; Li, S. Satellite-derived bathymetry using the ICESat-2 lidar and Sentinel-2 imagery datasets. *Remote Sens. Environ.* **2020**, *250*, 112047. [CrossRef]
12. Rossi, L.; Mammi, I.; Pelliccia, F. UAV-derived multispectral bathymetry. *Remote Sens.* **2020**, *12*, 3897. [CrossRef]
13. Alevizos, E.; Oikonomou, D.; Argyriou, A.V.; Alexakis, D.D. Fusion of drone-Based RGB and multi-spectral imagery for shallow water bathymetry inversion. *Remote Sens.* **2022**, *14*, 1127. [CrossRef]
14. Casella, E.; Collin, A.; Harris, D.; Ferse, S.; Bejarano, S.; Parravicini, V.; Hench, J.L.; Rovere, A. Mapping coral reefs using consumer-grade drones and structure from motion photogrammetry techniques. *Coral Reefs* **2017**, *36*, 269–275. [CrossRef]
15. Casella, E.; Lewin, P.; Ghilardi, M.; Rovere, A.; Bejarano, S. Assessing the relative accuracy of coral heights reconstructed from drones and structure from motion photogrammetry on coral reefs. *Coral Reefs* **2022**, *41*, 869–875. [CrossRef]
16. Chirayath, V.; Earle, S.A. Drones that see through waves–preliminary results from airborne fluid lensing for centimetre-scale aquatic conservation. *Aquat. Conserv. Mar. Freshw. Ecosyst.* **2016**, *26*, 237–250. [CrossRef]
17. Dietrich, J.T. Bathymetric Structure-from-Motion: Extracting shallow stream bathymetry from multi-view stereo photogrammetry. *Earth Surf. Process. Landforms* **2017**, *42*, 355–364. [CrossRef]
18. Pulido Mantas, T.; Roveta, C.; Calcinai, B.; di Camillo, C.G.; Gambardella, C.; Gregorin, C.; Coppari, M.; Marrocco, T.; Puce, S.; Riccardi, A.; et al. Photogrammetry, from the land to the sea and beyond: A unifying approach to study terrestrial and marine environments. *J. Mar. Sci. Eng.* **2023**, *11*, 759. [CrossRef]
19. David, C.G.; Kohl, N.; Casella, E.; Rovere, A.; Ballesteros, P.; Schlurmann, T. Structure-from-Motion on shallow reefs and beaches: potential and limitations of consumer-grade drones to reconstruct topography and bathymetry. *Coral Reefs* **2021**, *40*, 835–851. [CrossRef]
20. Fallati, L.; Saponari, L.; Savini, A.; Marchese, F.; Corselli, C.; Galli, P. Multi-Temporal UAV Data and object-based image analysis (OBIA) for estimation of substrate changes in a post-bleaching scenario on a maldivian reef. *Remote Sens.* **2020**, *12*, 2093. [CrossRef]
21. Agrafiotis, P.; Skarlatos, D.; Forbes, T.; Poullis, C.; Skamantzari, M.; Georgopoulos, A. Underwater photogrammetry in very shallow waters: Main challenges and caustics effect removal. *Int. Arch. Photogramm. Remote. Sens. Spat. Inf. Sci.* **2018**, *XLII-2*, 15–22. [CrossRef]
22. Agrafiotis, P.; Karantzalos, K.; Georgopoulos, A. Seafloor-Invariant Caustics Removal From Underwater Imagery. *IEEE J. Ocean. Eng.* **2023**, *48*, 1300–1321. [CrossRef]
23. Balletti, C.; Beltrame, C.; Costa, E.; Guerra, F.; Vernier, P. 3D reconstruction of marble shipwreck cargoes based on underwater multi-image photogrammetry. *Digit. Appl. Archaeol. Cult. Herit.* **2016**, *3*, 1–8. [CrossRef]
24. McCarthy, J.; Benjamin, J.; Winton, T.; Van Duivenvoorde, W. The rise of 3D in maritime archaeology. In *3D Recording and Interpretation for Maritime Archaeology*; Springer: Cham, Switzerland, 2019; pp. 1–10.
25. Reich, J.; Steiner, P.; Ballmer, A.; Emmenegger, L.; Hostettler, M.; Stäheli, C.; Naumov, G.; Taneski, B.; Todoroska, V.; Schindler, K.; et al. A novel Structure from Motion-based approach to underwater pile field documentation. *J. Archaeol. Sci. Rep.* **2021**, *39*, 103120. [CrossRef]
26. Rossi, P.; Castagnetti, C.; Capra, A.; Brooks, A.J.; Mancini, F. Detecting change in coral reef 3D structure using underwater photogrammetry: critical issues and performance metrics. *Appl. Geomat.* **2020**, *12*, 3–17. [CrossRef]
27. Remmers, T.; Grech, A.; Roelfsema, C.; Gordon, S.; Lechene, M.; Ferrari, R. Close-range underwater photogrammetry for coral reef ecology: a systematic literature review. *Coral Reefs* **2024**, *43*, 35–52. [CrossRef]
28. Raber, G.T.; Schill, S.R. Reef Rover: A Low-Cost Small Autonomous Unmanned Surface Vehicle (USV) for Mapping and Monitoring Coral Reefs. *Drones* **2019**, *3*, 38. [CrossRef]
29. Lange, I.D.; Perry, C.T. A quick, easy and non-invasive method to quantify coral growth rates using photogrammetry and 3D model comparisons. *Methods Ecol. Evol.* **2020**, *11*, 714–726. [CrossRef]

30. Bayley, D.T.I.; Mogg, A.O.M. A protocol for the large-scale analysis of reefs using Structure from Motion photogrammetry. *Methods Ecol. Evol.* **2020**, *11*, 1410–1420. [CrossRef]
31. Ventura, D.; Grosso, L.; Pensa, D.; Casoli, E.; Mancini, G.; Valente, T.; Scardi, M.; Rakaj, A. Coastal benthic habitat mapping and monitoring by integrating aerial and water surface low-cost drones. *Front. Mar. Sci.* **2023**, *9*, 1096594. [CrossRef]
32. Specht, M. Methodology for Performing Bathymetric and Photogrammetric Measurements Using UAV and USV Vehicles in the Coastal Zone. *Remote Sens.* **2024**, *16*, 3328. [CrossRef]
33. Ventura, D.; Mancini, G.; Casoli, E.; Pace, D.S.; Lasinio, G.J.; Belluscio, A.; Ardizzone, G. Seagrass restoration monitoring and shallow-water benthic habitat mapping through a photogrammetry-based protocol. *J. Environ. Manag.* **2022**, *304*, 114262. [CrossRef]
34. Solana Rubio, S.; Salas Romero, A.; Cerezo Andreo, F.; González Gallero, R.; Rengel, J.; Rioja, L.; Callejo, J.; Bethencourt, M. Comparison between the Employment of a Multibeam Echosounder on an Unmanned Surface Vehicle and Traditional Photogrammetry as Techniques for Documentation and Monitoring of Shallow-Water Cultural Heritage Sites: A Case Study in the Bay of Algeciras. *J. Mar. Sci. Eng.* **2023**, *11*, 1339. [CrossRef]
35. Nocerino, E.; Menna, F.; Gruen, A.; Troyer, M.; Capra, A.; Castagnetti, C.; Rossi, P.; Brooks, A.J.; Schmitt, R.J.; Holbrook, S.J. Coral Reef Monitoring by Scuba Divers Using Underwater Photogrammetry and Geodetic Surveying. *Remote Sens.* **2020**, *12*, 3036. [CrossRef]
36. Figueira, W.; Ferrari, R.; Weatherby, E.; Porter, A.; Hawes, S.; Byrne, M. Accuracy and Precision of Habitat Structural Complexity Metrics Derived from Underwater Photogrammetry. *Remote Sens.* **2015**, *7*, 16883–16900. [CrossRef]
37. Jaud, M.; Delsol, S.; Urbina-Barreto, I.; Augereau, E.; Cordier, E.; Guilhaumon, F.; Le Dantec, N.; Floc'h, F.; Delacourt, C. Low-Tech and Low-Cost System for High-Resolution Underwater RTK Photogrammetry in Coastal Shallow Waters. *Remote Sens.* **2023**, *16*, 20. [CrossRef]
38. Hatcher, G.A.; Warrick, J.A.; Kranenburg, C.J.; Ritchie, A.C. Accurate Maps of Reef-Scale Bathymetry with Synchronized Underwater Cameras and GNSS. *Remote Sens.* **2023**, *15*, 3727. [CrossRef]
39. Abadie, A.; Boissery, P.; Viala, C. Georeferenced underwater photogrammetry to map marine habitats and submerged artificial structures. *Photogramm. Rec.* **2018**, *33*, 448–469. [CrossRef]
40. Mauz, B.; Vacchi, M.; Green, A.; Hoffmann, G.; Cooper, A. Beachrock: A tool for reconstructing relative sea level in the far-field. *Mar. Geol.* **2015**, *362*, 1–16. [CrossRef]
41. Gewelt, M.; Fierro, G. Le beach-rock de Capo Noli (Finale Ligure, Italie): Datation 14C et variations diurnes du pH dans des cuvettes. *MOM Éditions* **1984**, *8*, 55–66.
42. Lau, L. Chapter 4—GNSS multipath errors and mitigation techniques. In *GPS and GNSS Technology in Geosciences*; Petropoulos, G.; Srivastava, P.K., Eds.; Elsevier: Amsterdam, The Netherlands, 2021; pp. 77–98. [CrossRef]
43. Hatcher, G.A.; Warrick, J.A.; Ritchie, A.C.; Dailey, E.T.; Zawada, D.G.; Kranenburg, C.; Yates, K.K. Accurate Bathymetric Maps From Underwater Digital Imagery Without Ground Control. *Front. Mar. Sci.* **2020**, *7*, 525. [CrossRef]
44. Lo, E.; Lozano Bravo, H.; Hui, N.; Nocerino, E.; Menna, F.; Rissolo, D.; Kuester, F. Evaluation of the Accuracy of Photogrammetric Reconstruction of Bathymetry Using Differential GNSS Synchronized with an Underwater Camera. *Int. Arch. Photogramm. Remote. Sens. Spat. Inf. Sci.* **2024**, *XLVIII-2-2024*, 211–218. [CrossRef]
45. Wang, H.; Zhang, W.; Ren, P. Self-organized underwater image enhancement. *ISPRS J. Photogramm. Remote Sens.* **2024**, *215*, 1–14. [CrossRef]
46. Boyden, P.; Weil-Accardo, J.; Deschamps, P.; O'Leary, M.; Rovere, A. Revisiting Battisitini: Refining Uncertainties in Classic Last Interglacial Field Sites. In Proceedings of the American Geophysical Union Fall Meeting 2019, San Francisco, CA, USA, 9–13 December 2019; p. PP24A–02.
47. Lyard, F.H.; Allain, D.J.; Cancet, M.; Carrère, L.; Picot, N. FES2014 global ocean tide atlas: Design and performance. *Ocean. Sci.* **2021**, *17*, 615–649. [CrossRef]
48. Raoult, V.; David, P.A.; Dupont, S.F.; Mathewson, C.P.; O'Neill, S.J.; Powell, N.N.; Williamson, J.E. GoPros™ as an underwater photogrammetry tool for citizen science. *PeerJ* **2016**, *4*, e1960. [CrossRef] [PubMed]
49. Casella, E.; Rovere, A. Data, Pre- and Post-processing scripts for shallow-water photogrammetry applications. *Zenodo* **2024**. [CrossRef]